



THE UNIVERSITY *of* EDINBURGH

Edinburgh Research Explorer

Use of DEM and elastic stability analysis to explain the influence of the intermediate principal stress on shear strength

Citation for published version:

O'Sullivan, C, Wadee, MA, Hanley, KJ & Barreto, D 2013, 'Use of DEM and elastic stability analysis to explain the influence of the intermediate principal stress on shear strength', *Géotechnique*, vol. 63, no. 15, pp. 1298-1309. <https://doi.org/10.1680/geot.12.P.153>

Digital Object Identifier (DOI):

[10.1680/geot.12.P.153](https://doi.org/10.1680/geot.12.P.153)

Link:

[Link to publication record in Edinburgh Research Explorer](#)

Document Version:

Publisher's PDF, also known as Version of record

Published In:

Géotechnique

General rights

Copyright for the publications made accessible via the Edinburgh Research Explorer is retained by the author(s) and / or other copyright owners and it is a condition of accessing these publications that users recognise and abide by the legal requirements associated with these rights.

Take down policy

The University of Edinburgh has made every reasonable effort to ensure that Edinburgh Research Explorer content complies with UK legislation. If you believe that the public display of this file breaches copyright please contact openaccess@ed.ac.uk providing details, and we will remove access to the work immediately and investigate your claim.



Use of DEM and elastic stability analysis to explain the influence of the intermediate principal stress on shear strength

C. O'SULLIVAN*, M. A. WADEE*, K. J. HANLEY* and D. BARRETO†

One interesting aspect of soil response is the sensitivity of the mechanical behaviour to the intermediate principal stress. In this study, a fundamental mechanism that explains the influence of the intermediate stress ratio (b) on soil shear strength is proposed. Prior experimental, numerical and analytical studies have indicated that soil failure occurs when the strong force chains that transmit stress through the material buckle. These strong force chains are networks of contacting particles that are relatively highly stressed, and aligned in the direction of the major principal stress (σ'_1). The buckling resistance is thought to be determined by 'weaker' lateral networks of less-stressed contacting particles that are orthogonal to the strong force chain orientation. Discrete-element method (DEM) simulations of true triaxial tests show that as b is varied, so too is the relative support provided by the force chains orientated in the directions of the intermediate and minor principal stresses (σ'_2 and σ'_3 respectively). At a macro scale, the effective axial stiffnesses along these directions vary. The DEM dataset is complex, and so a conceptually simple model is used to assess the influence of lateral support on the buckling resistance of a single column of connected nodes, analogous to a single force chain. The lateral support is modelled using linear springs. When the stiffnesses of these springs are selected to reflect the variation in axial stiffness with b observed in the DEM simulations, the reduction in axial buckling load with b is found to be similar to the reduction in major principal stress with b . When combined, the DEM data and simple analytical model support a hypothesis that failure under three-dimensional stress conditions is determined by buckling of the strong force chains. It is the variation in lateral support provided by the force network aligned along the minor and intermediate stress directions that determines, in part at least, the relation between soil shear strength and b . The data presented provide a conceptually simple framework to justify the need to consider three-dimensional effects in geomechanical stress–deformation analyses, and may inform future development of constitutive models.

KEYWORDS: anisotropy; discrete-element modelling; elasticity; particle-scale behaviour

INTRODUCTION

As a consequence of their particulate nature, granular materials exhibit some unique material response characteristics, including dilatancy, stress-dependency of strength and stiffness. The particular aspect of soil response considered in the current study is the sensitivity of soil shear strength to the anisotropy of the stress state. The stress anisotropy is quantified using the intermediate stress ratio

$$b = \frac{\sigma'_2 - \sigma'_3}{\sigma'_1 - \sigma'_3}$$

where σ'_1 , σ'_2 and σ'_3 are the major, intermediate and minor principal effective stresses respectively.

Early experimental studies documenting the influence of the b -value on soil response compared axisymmetric triaxial and plane-strain test results (e.g. Cornforth, 1964; Oda *et al.*, 1978; Marachi *et al.*, 1981). More systematic variation of b can be achieved using advanced testing apparatus, such as the true triaxial apparatus (e.g. Sutherland & Mesdary, 1969; Lade & Duncan, 1973), the hollow cylinder apparatus (e.g. Symes, 1983; Lade *et al.*, 2008), or the cubical cell

(e.g. Sadek, 2006). The angle of shearing resistance, given as

$$\phi' = \sin^{-1} \left(\frac{\sigma'_1 - \sigma'_3}{\sigma'_1 + \sigma'_3} \right)$$

is typically used as a measure of shear strength, and a general conclusion of these studies is that the peak ϕ' value tends to increase as b increases from axisymmetric triaxial compression conditions ($b = 0$), to achieve a maximum value at around plane strain (where b is about 0.3–0.5), and decreases until b attains a maximum value of 1.0 (axisymmetric triaxial extension). Various failure criteria have been proposed that define relationships between the three principal stresses at failure. Fig. 1 compares the failure criteria proposed by Ogawa *et al.* (1974), Satake (1975), Lade (1977, 1984) and Matsuoka & Nakai (1978), for a mean effective stress (p') of 200 kPa; for each criterion the parameters that best fitted the DEM simulations on Specimen A (ellipsoidal particles) described by Ng (2004) were used. Fig. 1(a) illustrates the variation in the peak ϕ' with b , and Fig. 1(b) gives the variation in σ'_1 with b , normalised by the maximum σ'_1 obtained for that criterion. Although these experimental studies and failure criteria demonstrate the sensitivity of shear strength to b , they do not explain the fundamental mechanisms. In situ soils are subject to a three-dimensional (3D) stress state, and so a fundamental understanding is important.

Experiments using both photoelastic discs (Drescher & de Josselin de Jong, 1972) and DEM simulations (Rothenburg

Manuscript received 10 October 2012; revised manuscript accepted 17 April 2013. Published online ahead of print 17 July 2013. Discussion on this paper closes on 1 May 2014, for further details see p. ii.

* Department of Civil and Environmental Engineering, Imperial College London, UK.

† School of Engineering and the Built Environment, Edinburgh Napier University, UK.

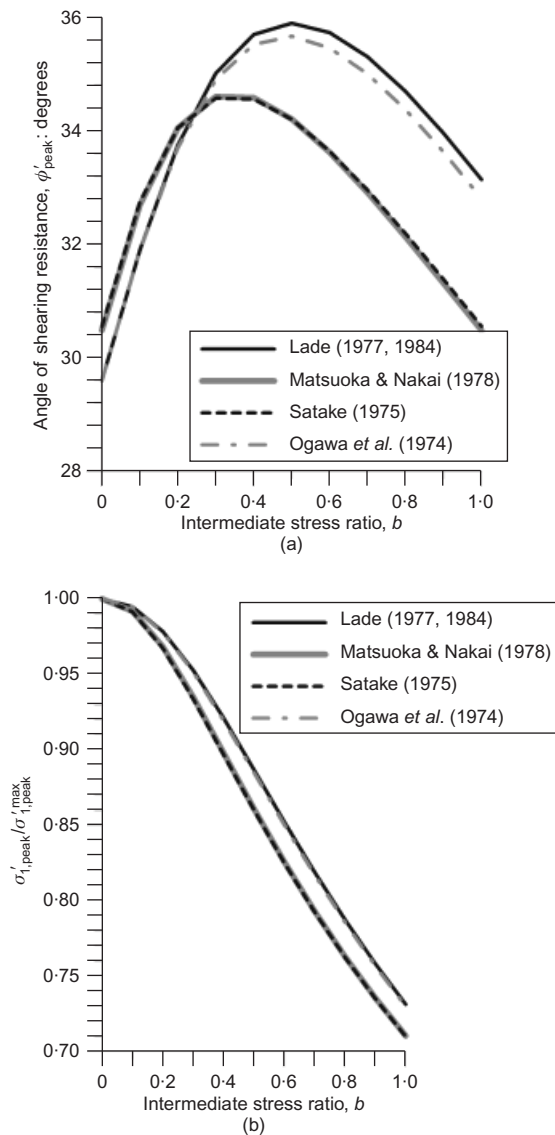


Fig. 1. Comparison of four failure criteria using parameters determined by Ng (2004): (a) peak angle of shearing resistance (ϕ'_{peak}) against b ; (b) peak value of major principal stress, normalised by its overall peak value, against b

& Bathurst, 1989) have shown that the distribution of contact forces within a stressed granular material is heterogeneous and complex. It is therefore not easy to infer fundamental, particle-scale mechanisms governing soil response directly from photoelastic or DEM datasets. However, despite the complexity, it is clear that strong force chains or load-carrying columns of relatively highly stressed particles form, with orientations approximately parallel to the major principal stress orientation. As a material is deformed or loaded, these force chains collapse or buckle.

In the current work, we use DEM data and a simple analytical model to support an argument that it is the failure of the material due to buckling of the strong force chains that determines the sensitivity of soil shear strength to b . In particular, the lateral support to the strong chains, provided by the weaker force network aligned along the minor and intermediate stress directions, varies with b . The paper first summarises the results of a series of DEM simulations of true triaxial compression to show how the lateral support varies at the particle scale; then a simple non-linear model comprising a single vertical force chain laterally supported by horizontal springs is described. The lateral spring stiff-

nesses in the simple model are selected to match the variation in axial stiffnesses along the minor and intermediate principal stress directions observed in the DEM simulations. The variation in the minimum axial buckling load with b is shown to be similar to the variation in peak σ'_1 with b . The data presented indicate that the mechanism of buckling of strong force chains may explain the sensitivity of soil shear strength to the intermediate principal stress ratio. The analytical model also provides a simple framework to justify the need to consider 3D effects in geomechanical stress–deformation analyses, and may aid in the future development of fully 3D constitutive models.

DEM SIMULATIONS

The DEM simulations are also described by Barreto (2009) and Barreto & O'Sullivan (2012); however, in the interests of clarity, an overview is given here. The DEM code used is a modified version of TRUBAL (Cundall & Strack, 1979). Contact was modelled with a simplified Hertz–Mindlin model, taking the Poisson's ratio to be 0.22, the shear modulus to be 28.68 GPa, and the particle density to be 2570 kg/m³. The particle size distribution matched that of the glass ballotini particles considered in the experimental work of Barreto (2009); seven different particle sizes between 1.005 mm and 1.425 mm were used, giving a mean particle diameter (d_{50}) of 1.1 mm. Isotropic specimens were created in a periodic cell by monotonically compressing an initial configuration of 4000 non-contacting spheres to a stress of 200 kPa, giving a void ratio, $e = 0.521$. For each true triaxial test simulation, a servo-controlled algorithm was used to maintain both the mean effective stress (p') and b constant while the sample was compressed in the σ'_1 (z) direction. In the current study, data from two series of simulations using differing interparticle friction values ($\mu = 0.14$ and $\mu = 0.325$) are examined, and each series includes ten simulations with b values of 0, 0.1, 0.2, 0.3, 0.4, 0.5, 0.6, 0.8, 0.9 and 1. Referring to Figs 2 and 3, the observed responses are in general agreement with the failure criteria illustrated in Fig. 1.

The material shear strength is quantified using the maximum value of ϕ' : that is, ϕ'_{peak} , as illustrated in Fig. 2. The data indicate an increase in ϕ'_{peak} as b increases from 0 (axisymmetric compression) to about 0.5 (close to plane-

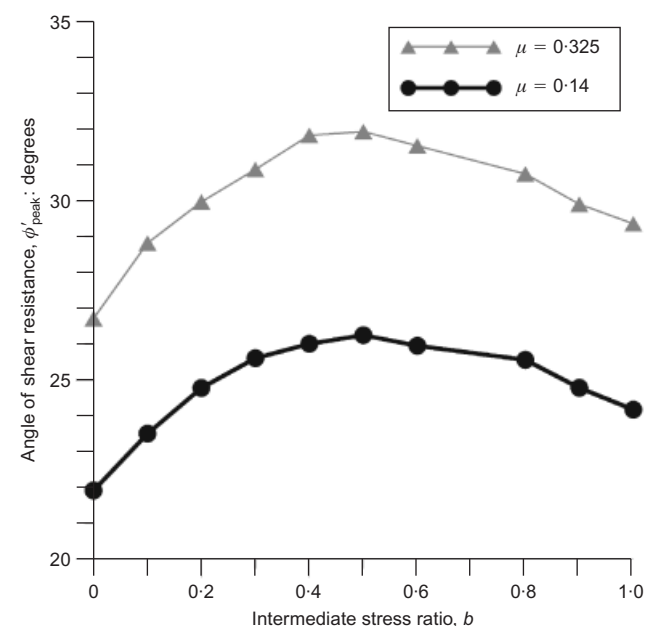


Fig. 2. Peak angle of shearing resistance (ϕ'_{peak}) against b

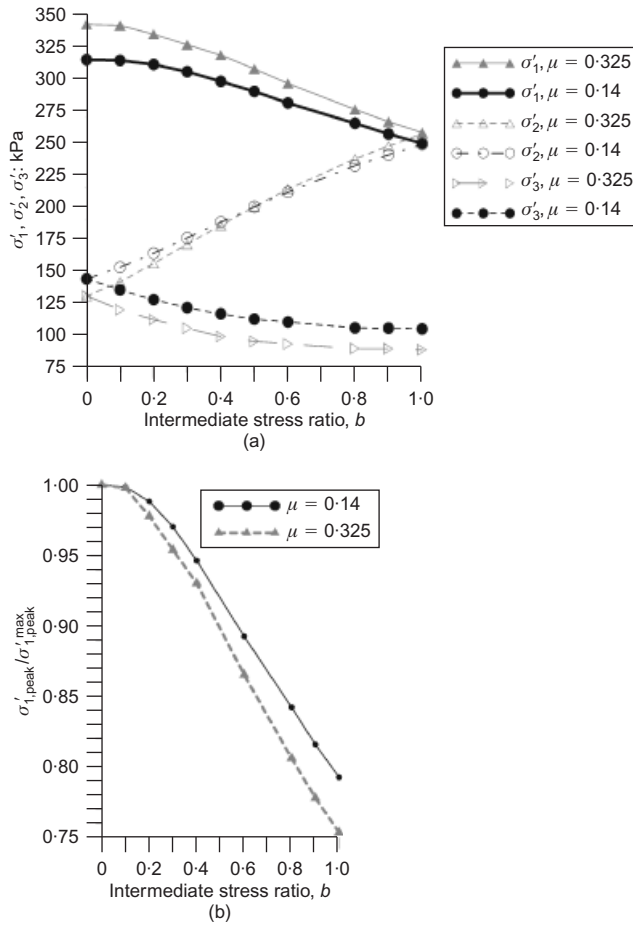


Fig. 3. (a) Values of σ'_1 , σ'_2 and σ'_3 when $\phi' = \phi'_{peak}$ for DEM simulations run using friction coefficients of 0.14 and 0.325 for range of b values between 0 and 1; (b) peak value of major principal stress, normalised by its overall peak value for friction coefficients of 0.14 and 0.325, against b

strain compression), and there is a subsequent decrease as b increases further to its maximum value of 1 (axisymmetric extension). As discussed by Barreto & O'Sullivan (2012), this variation in b corresponds with the results of the earlier DEM simulations of Thornton (2000) and Ng (2004). Not all experimental studies have observed the decrease in ϕ'_{peak} for b values above 0.5; for example, the data from Haruyama (1981) are in agreement, whereas the data from Shapero & Yamamuro (2003) are not. The peak stress values obtained in the simulations gave a good fit to the failure envelope proposed by Lade & Duncan (1975), and the η parameter that determines the position of this strength envelope in 3D stress space was found to depend on μ (Barreto & O'Sullivan, 2012). Fig. 3(a) illustrates the variation of the principal stress values corresponding to the ϕ'_{peak} data in Fig. 2; there is a systematic decrease in the σ'_1 value, a less marked decrease in σ'_3 , and a systematic increase in σ'_2 . During the simulations, the lateral sample deformation (along the σ'_2 (y) and σ'_3 (x) directions) is controlled to maintain a constant mean stress and the stated b -value. Clearly, there is an interplay between the resultant variations in σ'_2 and σ'_3 and the peak value of σ'_1 ($\sigma'_{1,peak}$) mobilised in axial compression. Fig. 3(b) plots the σ'_1 data in normalised form, and the rate at which σ'_1 decreases with b is seen to be sensitive to the interparticle friction coefficient.

Some insight into the mechanisms governing the systematic variation can be obtained by reference to Figs 4–6. Fig. 4 illustrates the projection of the contact force network onto three orthogonal slices, each bisecting the periodic cell, for

the initial case at the start of compression and at a strain level close to the point where ϕ'_{peak} is mobilised for b values of 0, 0.4 and 1, with $\mu = 0.325$. The lines drawn between the centroids of contacting particles are distinguished as being 'strong' or 'weak', depending on whether the contacts transmit forces that are greater than or less than the average force. The strong force chains that form along the major principal stress orientation are clearly visible as the thicker grey lines in the x – z and y – z projections. The force network in the XY plane can act as a prop to the strong force chains; prior recognition of the supporting role of lateral contacts was given by Tordesillas & Muthuswamy (2009), among others. Clearly, there are several horizontally oriented strong forces, and these seem to develop an increased bias in the σ'_2 (y) direction as b increases. This qualitative observation is confirmed in the polar histogram of the horizontal (xy) projections of the contact orientations considering the entire set of contacts, presented in Fig. 5. Each histogram bin is shaded according to the magnitude of average force orientated in that bin. As b increases, there is an increase both in the number of contacts orientated in the σ'_2 (y) direction, and in the magnitude of the associated contact forces, relative to the contacts that have an orientation in the σ'_3 (x) direction. As a Hertzian contact model is used, the increase in force acting in the y -direction will cause an increase in stiffness of the effective lateral support acting in this direction. An additional increase in macro-scale stiffness will also be caused by the increased number of contacts orientated in this direction. It therefore seems plausible that the variation in support provided by these lateral contacts may explain the variation in the peak σ'_1 values.

More quantitative insight can be achieved by looking at averaged parameters in the system. Assuming that the contacts transmitting greater-than-average forces are those most likely to participate in the strong force chains (Thornton & Antony, 1998; Barreto & O'Sullivan, 2012), a strong force second-order fabric tensor can be calculated as

$$\Phi_{ij}^s = \frac{1}{N_c^s} \sum_{k=1}^{N_c^s} n_i n_j$$

where N_c^s is the number of contacts transmitting forces whose magnitude exceeds the average value, and n_i ($i = 1, 2, 3$) is the unit vector describing the contact normal orientation. The eigenvalues of this tensor then give an indication of the preferential orientations along the major, intermediate and minor axes, Φ_1^s , Φ_2^s and Φ_3^s respectively. For the spherical particles considered here, the principal fabric orientations and the principal stress orientations coincide. Fig. 6 considers the principal fabric components along the three principal axes and their variation during the test simulations as a function of deviatoric strain. Comparing Figs 6(b) and 6(c), it is clear that as the b -value increases, so too does the difference between the values of Φ_2^s and Φ_3^s . These data also suggest that the support provided along the minor principal stress direction decreases significantly, relative to the support provided along the intermediate principal stress direction. Further analysis of the anisotropy of the contact force network is provided by Barreto & O'Sullivan (2012).

The stress–strain responses along the three principal stress directions were then analysed to examine the influence on the effective axial stiffnesses during the compression tests. The secant stiffnesses in the direction of the intermediate and minor principal stress were calculated at axial strains along the major principal stress direction of $\epsilon_a = 0.1\%$ and 1% . It seems reasonable to argue that these stiffnesses give a measure of the support provided to the strong force chains that develop along the major principal stress direction (z -

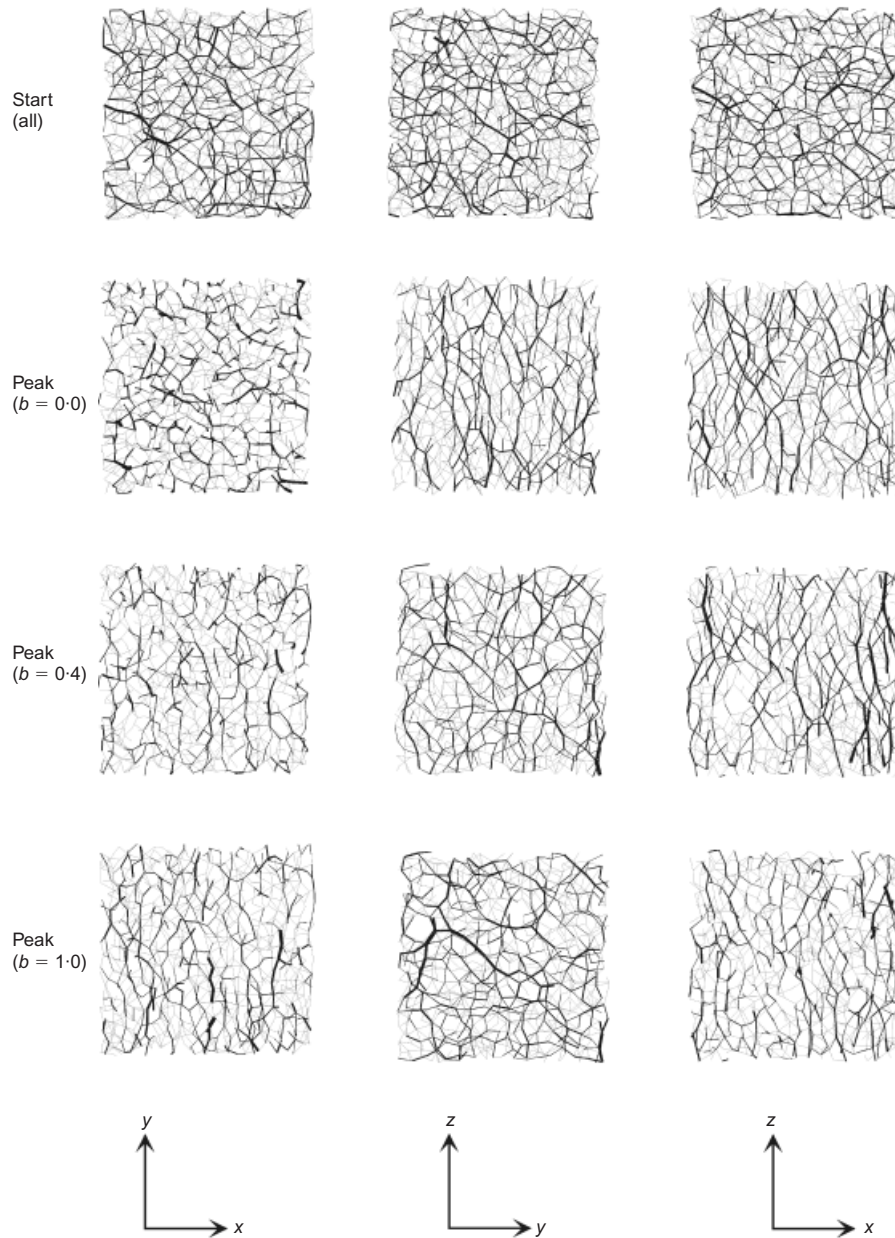


Fig. 4. Effect of b on strong force network ($\mu = 0.325$)

axis). Normalised values of these stiffnesses are presented in Fig. 7. Fig. 7(a) gives the ratio E_y/E_x , and Fig. 7(b) looks at the sum of the two stiffnesses, normalised by the maximum sum for that combination of axial strain

$$\frac{E_x + E_y}{(E_x + E_y)_{\max}}$$

The variation is non-trivial, and the ratio E_y/E_x increases from unity for an isotropic condition to obtain a maximum value at about $b = 0.4$; it then decreases to an isotropic state again, and increases as b approaches 1 (axisymmetric extension). Very similar variations are observed for the two interparticle friction values used and the two strain levels considered. The material is inherently non-linear, and the variation in octahedral stiffness with strain is documented in Barreto & O'Sullivan (2012). Referring to Fig. 7, the sum

$$\frac{E_x + E_y}{(E_x + E_y)_{\max}}$$

increases from the axisymmetric compression state ($b = 0$) to attain a maximum value as the plane-strain case is approached. Thereafter, the sum shows a significant reduction, and continues to decrease as axisymmetric extension conditions are approached.

When taken in combination, the data presented in Figs 4–7 show, qualitatively at the particle scale and quantitatively at the element scale, that as b varies, the lateral support provided to the strong force chains also varies. Tordesillas & Muthuswamy (2009) argue that this lateral support provides resistance to buckling of the strong force chains. Thus it seems logical to argue that the variation in shear strength with b is a manifestation of the variation of this lateral support. To explore this hypothesis, a conceptually simple buckling model was developed and analysed.

DEVELOPMENT OF BUCKLING MODEL

As noted above, the existence of strong force chains in granular materials – that is, connected particles transmitting relatively large forces – has been known since photoelastic

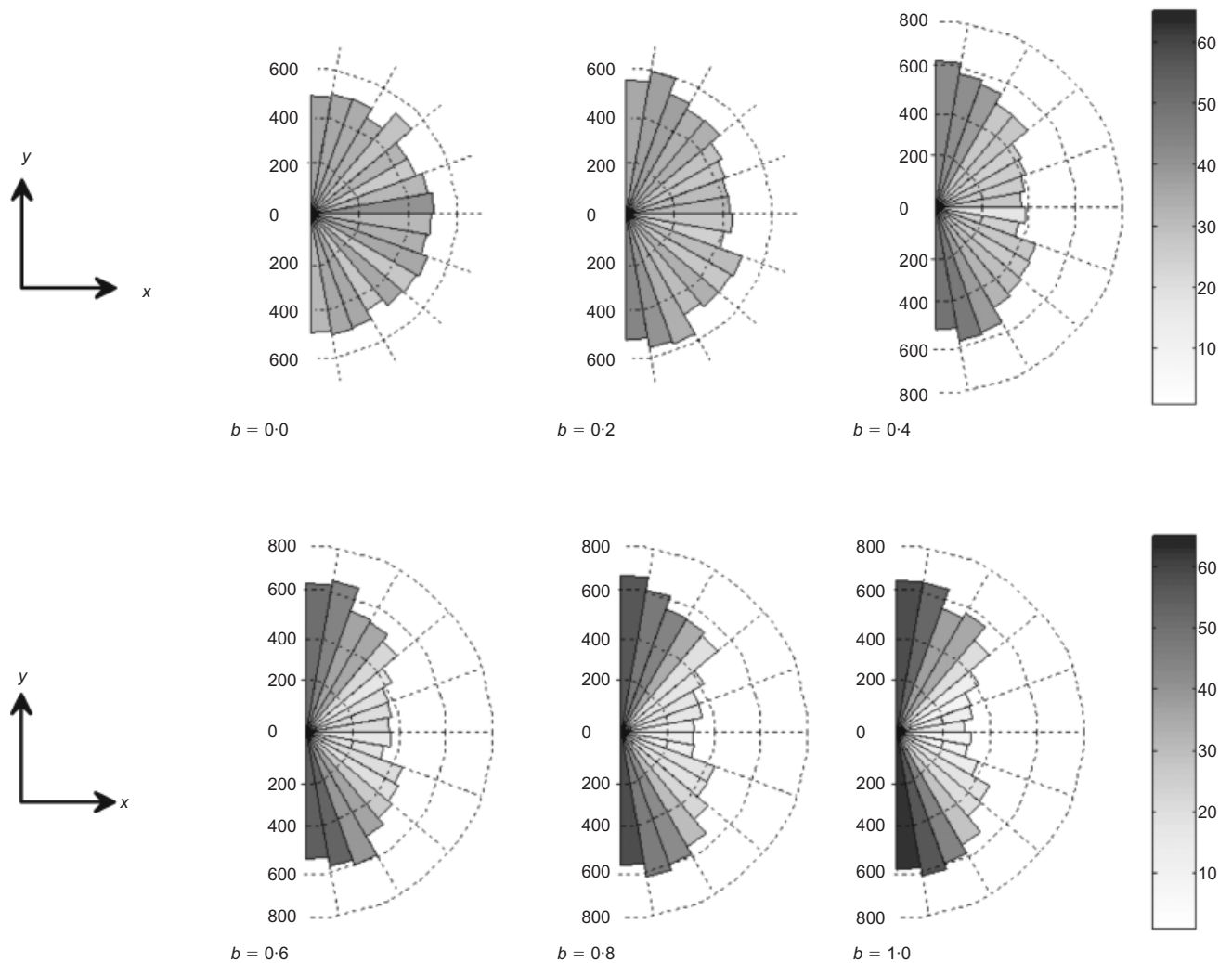


Fig. 5. Polar histograms of contact forces in xy plane; shading illustrates average magnitude of contact forces with orientations within each histogram bin ($\mu = 0.325$)

studies in the 1970s (e.g. Drescher & de Josselin de Jong, 1972). Analysis of later photoelastic and two-dimensional (2D) DEM datasets led to the association of overall material failure with collapse of the strong force chains, and the use of the term ‘buckling’ to describe such a collapse (Iwashita & Oda, 1998; Oda & Kazama, 1998; Oda *et al.*, 1998). More recently, Hasan & Alshibli (2010) observed such force chains in shear bands in sand directly, using high-resolution microcomputed tomography. Rechenmacher *et al.* (2010) inferred the occurrence of force chain collapse in a shear band in sand subject to plane-strain compression, using digital image correlation. These ideas have become accepted by many researchers, with Tordesillas (2007) arguing that buckling of the strong force chains is ‘well recognised’ as a meso-scale mechanism of granular material failure. Tordesillas then analysed DEM simulation results, considering energy dissipation, particle rotations and translations, and presented schematic diagrams of various buckling scenarios.

Strictly speaking, from a structural mechanics perspective, buckling is a mathematical instability caused by a bifurcation in the solution to the equations of static equilibrium. An analytical framework to study the phenomenon of slender columns buckling under axial loading was originally proposed by Euler (1744). To demonstrate that the conventional approaches to analyse buckling in structural mechanics are applicable in granular materials, Tordesillas & Muthuswamy (2009) proposed a simple, structural 2D model, analogous to a strong force chain, that comprises either perfect, or slightly

imperfect, vertical columns of contacting discs. Disc–disc contact was modelled using linear penalty springs. The stabilising contribution of the lateral force network was included by using horizontal springs attached to the disc centroids (excluding those at the top and bottom boundaries). An expression for the total potential energy stored in the system was developed as a function of the contact and lateral spring stiffnesses, the particle displacements and translations, the axial displacement of the column, and the applied axial force. By adopting an energy-based analysis of stability, and setting the partial derivative of the expression for the potential energy with respect to the disc motions equal to zero, the axial force causing buckling can be obtained. Tordesillas & Muthuswamy (2009) then showed that such a three-node model could predict buckling response observed in 2D DEM simulations, and provide an explanation for the relationship between granular material strength and confining pressure. Extending these ideas, Tordesillas *et al.* (2011) applied an energy-based approach to a lattice model to simulate collective buckling, and study stress–dilatancy.

Of particular relevance to the current study is the ‘spring and rigid link’ model proposed by Hunt *et al.* (2010), and illustrated in Fig. 8. In this model, a single (vertical) force chain is idealised as a series of nodes connected by rigid links (each of length L), and supported by linear lateral springs with stiffness k_f (to simulate the lateral supporting weak force network), and rotational springs with stiffness k_r .

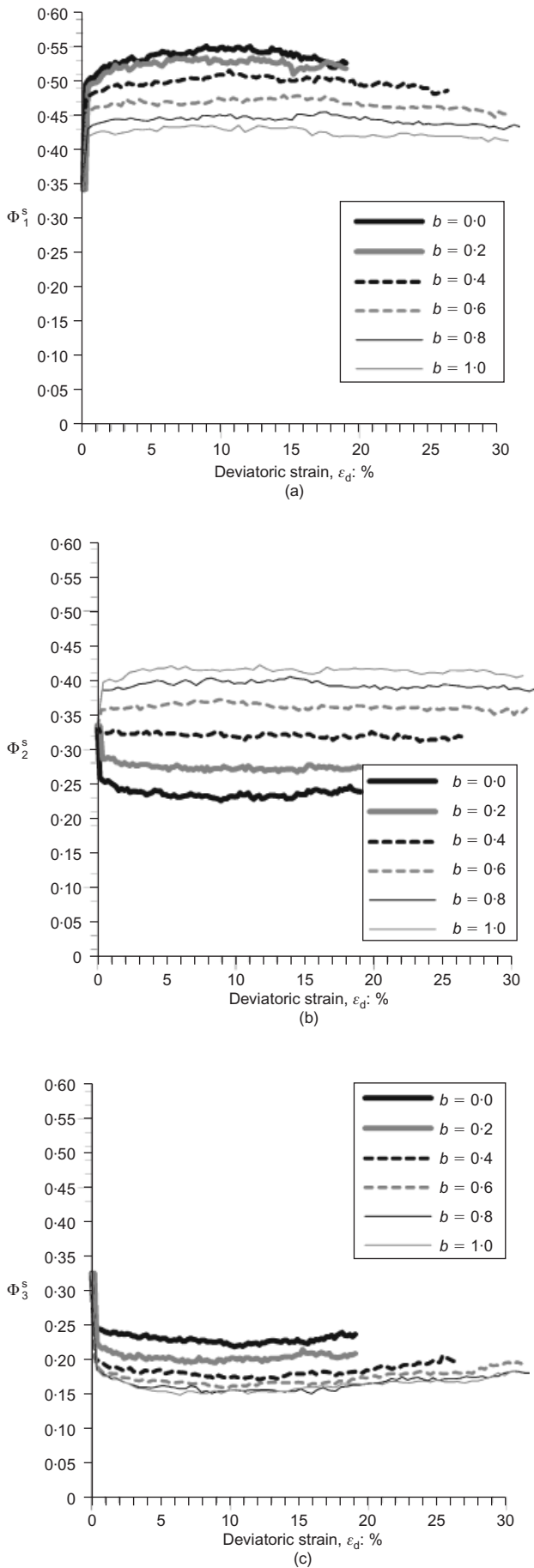


Fig. 6. Principal strong fabric components plotted against deviatoric strain: (a) major component, Φ_1^s ; (b) intermediate component, Φ_2^s ; (c) minor component, Φ_3^s ($\mu = 0.325$)

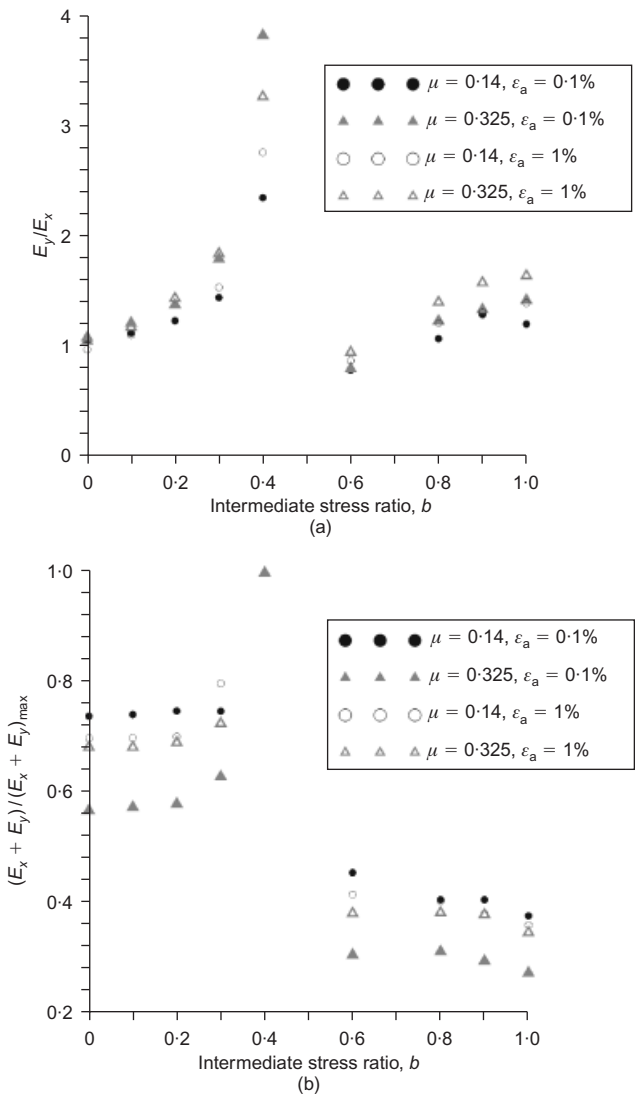


Fig. 7. (a) Ratio of lateral secant stiffnesses (E_y/E_x) against b for axial strains of 0.1% and 1% for $\mu = 0.14$ and 0.325; (b) normalised sums of lateral stiffnesses against b for axial strains of 0.1% and 1% for $\mu = 0.14$ and 0.325

These rotational springs simulate the rotational resistance provided by the shear component of the contact force where friction is non-zero (even in the case of spherical particles). Where the particles are non-spherical, the branch vectors and contact vectors are not collinear, and so the normal component of the contact force induces a moment and rotational resistance. For irregularly shaped grains, multiple contacts can occur and the contact areas will be finite, providing additional resistance. In the general case of N nodes and $N + 1$ links there are N degrees of freedom in the system, and in its deflected state each node i can move horizontally a distance of $q_i L$, where q_i is a proportionality factor that depends on the buckling mode, as illustrated in Fig. 8. As outlined by Hunt *et al.* (2010), the use of one translational degree of freedom per node is justified, as, in line with the observations of Tordesillas & Muthuswamy (2009), the two factors providing resistance to force chain buckling are rotational resistance at contacts between particles along the force chain and lateral support provided by orthogonal ‘weaker’ force chains. The key basic assumptions are that the nodal deflections and rotations always increase, and that they are in the small displacement range and so are linear elastic.

In the current study, the model proposed by Hunt *et al.* (2010) was extended to three dimensions, as illustrated

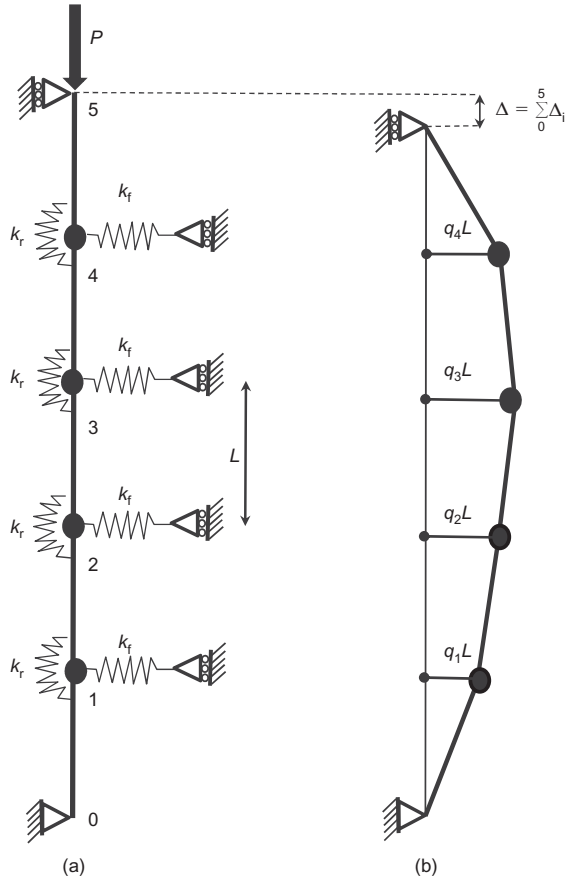


Fig. 8. Schematic diagram of 2D spring and link model proposed by Hunt *et al.* (2010)

schematically in Fig. 9 for the three-node case. As before in the general case, the model consists of N nodes that are connected by $N + 1$ rigid links, each of length L . Each node is supported by four springs: two linear springs in the x - and y -directions, with stiffnesses k_{fx} and k_{fy} ; and two rotational springs around the x - and y -directions, with stiffnesses k_{rx} and k_{ry} . The other ends of the linear springs are attached to frictionless slider elements. The first link is pin-jointed at the point designated as 0 in Fig. 9, and a load P is applied to the upper link (at point number 4 in Fig. 9).

The displacements of any node i in the x - and y -directions from its undeflected state with unstressed springs are given by $q_{ix}L$ and $q_{iy}L$ respectively, where q_{ix} and q_{iy} are proportionality factors depending on the buckling mode, as before. This 3D model therefore has a total of $2N$ translational degrees of freedom: N degrees of freedom following the x -direction, and N following the y -direction. Motion in the vertical direction is not explicitly considered; rather it is included by considering the work done during deflection.

Potential energy function of the system

Following the approach of Thompson & Hunt (1973) and Hunt *et al.* (2010), a total potential energy function V can be developed by considering the elastic potential energy of the linear elastic lateral springs (U_L), the elastic potential energy of the rotational springs (U_R), and the work done by the load P ($P\Delta$): that is

$$V = U_L + U_R - P\Delta \quad (1)$$

The U_L term can be developed by considering that, after buckling, each of the nodes moves in its xy (i.e. horizontal) plane, causing compression of the $2N$ linear springs linking

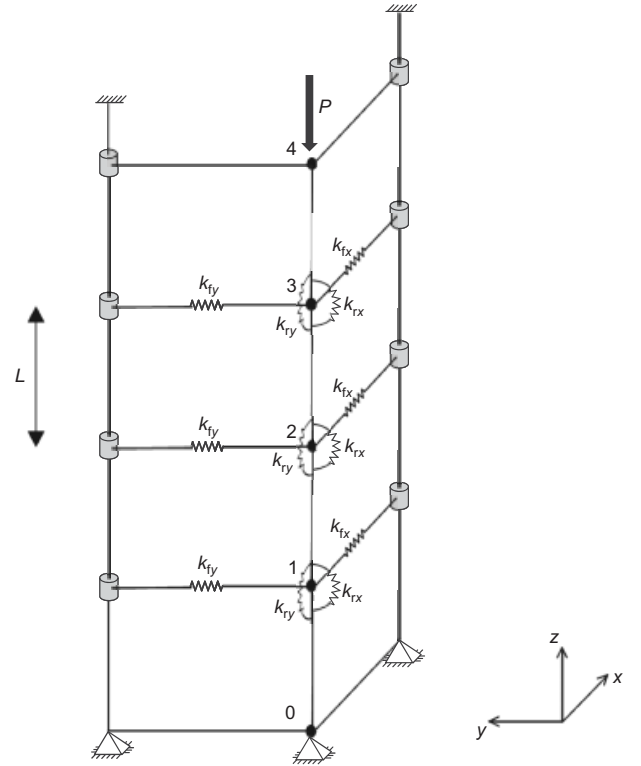


Fig. 9. 3D spring and link model with three nodes in undeflected state with unstressed lateral and rotational springs

the N nodes, and hence the strain energy within the springs increases. The respective compressive lengths of the two horizontal springs are given by $L\sqrt{(q_{yi}^2 + (1 - q_{xi})^2)}$ and $L\sqrt{(q_{xi}^2 + (1 - q_{yi})^2)}$, as shown in Fig. 10. The total elastic potential energy (i.e. strain energy) stored in the $2N$ linear springs is then given by

$$U_L = \frac{1}{2}k_{fx}L^2 \sum_{i=1}^N \left[1 - \sqrt{q_{yi}^2 + (1 - q_{xi})^2} \right]^2 + \frac{1}{2}k_{fy}L^2 \sum_{i=1}^N \left[1 - \sqrt{q_{xi}^2 + (1 - q_{yi})^2} \right]^2 \quad (2)$$

In the buckling process, the $N + 1$ rigid links lose their vertical alignment, the angle θ_i (between the links i and $i + 1$) is no longer zero, and the $2N$ rotational springs

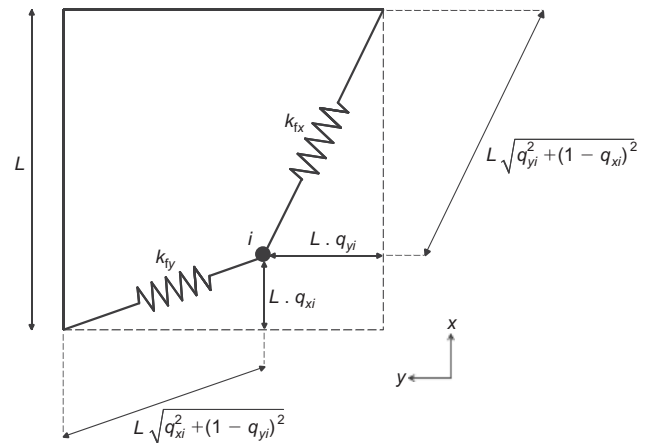


Fig. 10. Computation of elastic potential energy of linear lateral springs in 3D

also store strain energy. As illustrated in Fig. 11, the angles θ_{xi} and θ_{yi} are the projections of the angle θ_i on the yz and xz planes respectively. If the angles α_x and β_x are given by

$$\alpha_x = \sin^{-1}(q_{yi+1} - q_{yi}) \quad (3)$$

$$\beta_x = \sin^{-1}(q_{yi} - q_{yi-1}) \quad (4)$$

then θ_{xi} is

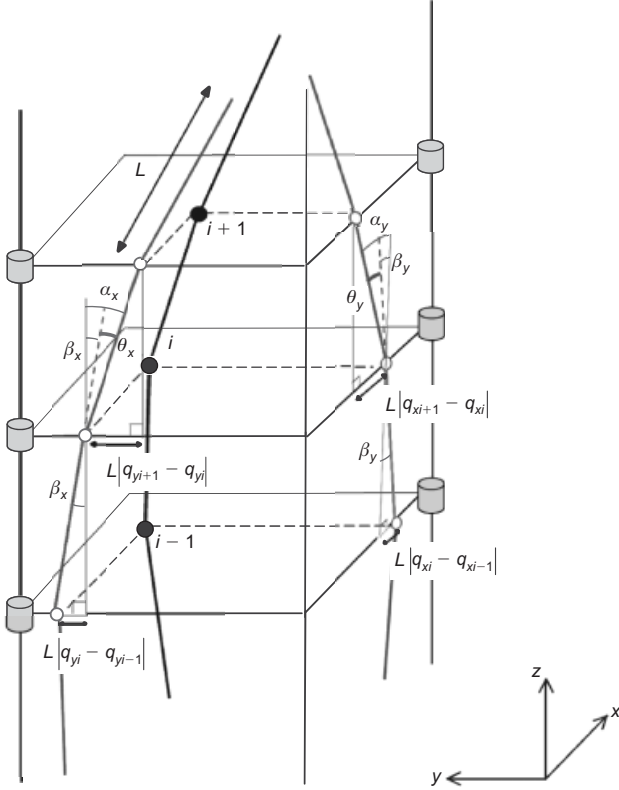


Fig. 11. Computation of angles of rotation, θ_{xi} and θ_{yi}

$$\begin{aligned} \theta_{xi} &= \alpha_x - \beta_x \\ &= \sin^{-1}(q_{yi+1} - q_{yi}) - \sin^{-1}(q_{yi} - q_{yi-1}) \end{aligned} \quad (5)$$

Using similar logic, it follows that

$$\theta_{yi} = \sin^{-1}(q_{xi+1} - q_{xi}) - \sin^{-1}(q_{xi} - q_{xi-1}) \quad (6)$$

The total strain energy stored in the rotational springs is

$$\begin{aligned} U_R &= \frac{1}{2} k_{rx} \sum_{i=1}^N [\sin^{-1}(q_{yi+1} - q_{yi}) - \sin^{-1}(q_{yi} - q_{yi-1})]^2 \\ &\quad + \frac{1}{2} k_{ry} \sum_{i=1}^N [\sin^{-1}(q_{xi+1} - q_{xi}) - \sin^{-1}(q_{xi} - q_{xi-1})]^2 \end{aligned} \quad (7)$$

The work done by the external load is the product of the total vertical shortening, Δ , of the loaded system and P . Referring to Fig. 12, the vertical displacement of the i th rigid link can be related to the lateral displacements by

$$\Delta_i = L \left(1 - \sqrt{1 - \left(\sqrt{q_{xi+1}^2 + q_{yi+1}^2} - \sqrt{q_{xi}^2 + q_{yi}^2} \right)^2} \right) \quad (8)$$

and so

$$\begin{aligned} P\Delta &= P \sum_{i=0}^N \Delta_i \\ &= PL \sum_{i=0}^N \left(1 - \sqrt{1 - \left(\sqrt{q_{xi+1}^2 + q_{yi+1}^2} - \sqrt{q_{xi}^2 + q_{yi}^2} \right)^2} \right) \end{aligned} \quad (9)$$

Note that $q_{x0} = q_{y0} = q_{x(N+1)} = q_{y(N+1)} = 0$.

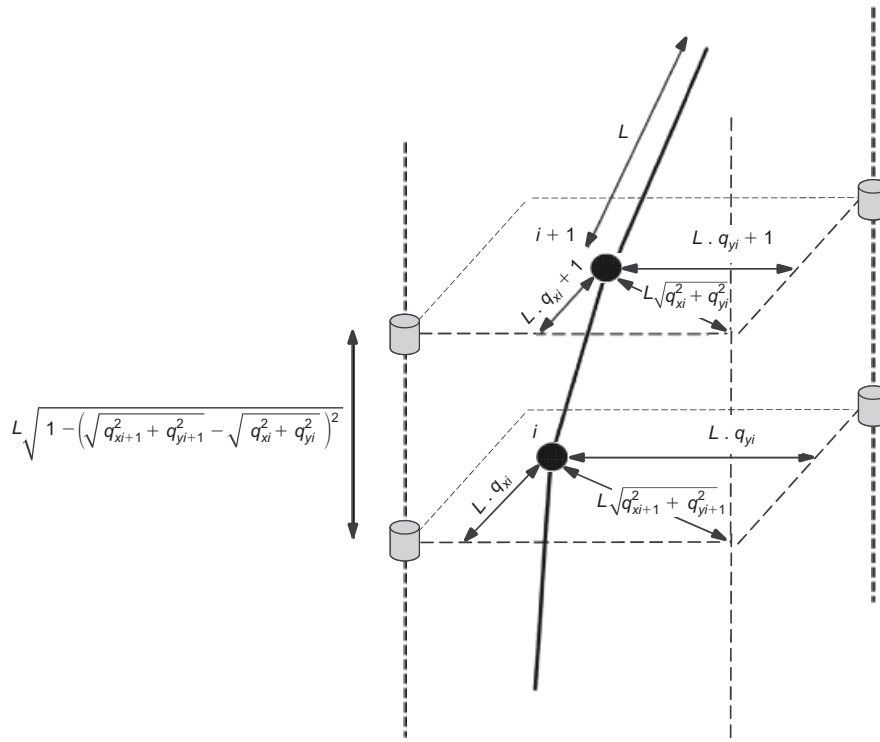


Fig. 12. Computation of vertical shortening between a pair of adjacent nodes, i and $i + 1$, in 3D

At equilibrium, the potential energy is stationary; energy dissipation due to friction or particle breakage is neglected in this simple analogue. For the three-node case, this statement is equivalent to the following system of equations

$$\frac{\partial V}{\partial q_{xi}} = \frac{\partial V}{\partial q_{yi}} = 0 \quad (10)$$

where $i = 1, 2, \dots, N$, and noting that $V = f(q_{x1}, q_{x2}, \dots, q_{xN}, q_{y1}, q_{y2}, \dots, q_{yN}, k_{fx}, k_{fy}, k_{tx}, k_{ty}, L, P)$. In the case of the seven-node model that was also considered in the current study, a system of 14 equilibrium equations was generated.

For both the three-node and seven-node systems considered here, the required partial derivatives of the potential energy function were calculated symbolically using Maple 15.01 (Maplesoft, 2011). The CodeGeneration package within Maple was used to generate a Fortran equations file suitable for input to AUTO-07p (Doedel & Oldeman, 2009). AUTO-07p was developed primarily for continuation and bifurcation analysis of solutions of systems of ordinary differential and algebraic equations. In the current study, AUTO-07p was used to compute bifurcation points and compute branches of stable and unstable solutions. For each model evaluation, the failure load, P^C , was taken as the first non-trivial bifurcation point on the fundamental path.

Application of buckling model

The objective of the buckling analysis was to assess whether qualitative agreement between the results of the DEM simulations and the buckling model could be obtained. Given the simplicity of the model, selecting parameters that would quantitatively match features in the DEM model was deemed inappropriate. The link length, L , was set to be unity for all model evaluations. In all cases an unperturbed (perfect) system was analysed (i.e. the initial displacements of the nodes were zero in all cases with $q_{xi} = q_{yi} = 0$ for all i). A parametric study was carried out in which the spring stiffness values ($k_{fx}, k_{fy}, k_{tx}, k_{ty}$) were systematically varied. Combinations of k_{fx} and k_{fy} were selected that matched the relative values of E_x and E_y observed in the DEM simulations. As illustrated in Fig. 13(a), the ratios k_{fx}/k_{fy} were selected to match the ratios of E_y/E_x given in Fig. 7(a), and the sums $(k_{fx} + k_{fy})/\gamma$ are largely in agreement with the values of $(E_x + E_y)/(E_x + E_y)_{\max}$ illustrated in Fig. 7(b). Taking the proportionality factor γ to have values of 1, 5 or 10, the required k_{fx} and k_{fy} values could easily be determined. In the absence of any simple, meaningful procedure to measure k_{tx} and k_{ty} , in all analyses $k_{tx} = k_{ty}$, and values of $k_{tx} = k_{ty} = 0.2, 0.4, 0.5, 0.8$ and 1.0 were considered.

Figure 14 presents the values of the minimum buckling load (P^C) obtained for a series of three-node and seven-node analyses with γ set equal to 1, 5, and 10, and $k_{tx} = k_{ty} = 0.5$ in all cases. Since the comparison is qualitative, the P^C values for a set of analyses with a given γ value and number of nodes were normalised by the maximum P^C value for that analysis set. The resulting variation in P^C is similar to the variation in $\sigma'_{1,\text{peak}}$ presented in Figs 1(b) and 3(b). The maximum P^C value is observed at $b = 0$ in all cases, and there is a systematic reduction in the buckling load as b increases. The nature of the variation is not as smooth as was observed in the true triaxial simulations, and the rate of variation of P^C with b varies with the proportionality parameter, γ . Fig. 15(a) presents data using the normalisation approach adopted in Fig. 14; however, in this case the rotational stiffnesses, k_{tx} and k_{ty} , were varied, and again the rate of variation of P^C with b is found to be sensitive to the rotational spring stiffnesses. In Fig. 15(b) the P values are normalised by the maximum P^C value for the entire set

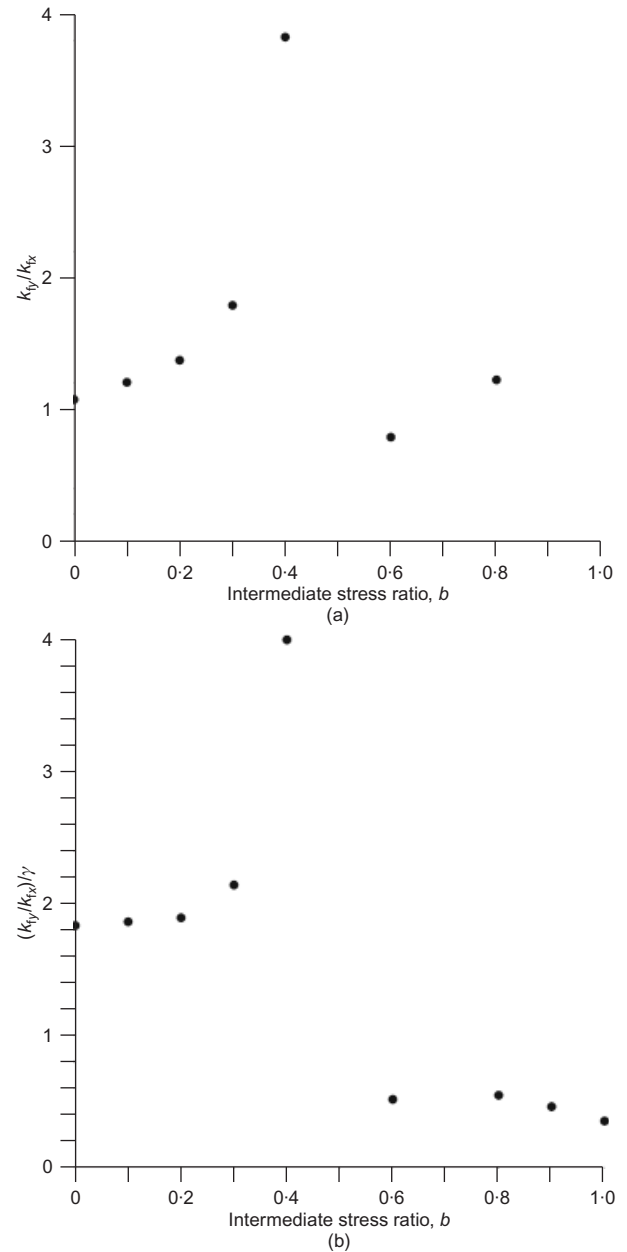


Fig. 13. Values for linear spring used in elastic buckling analysis: (a) variation in ratio k_{fy}/k_{fx} with b ; (b) variation in normalised sum $(k_{fy} + k_{fx})/\gamma$ for $\gamma = 5$

of data considered, and P^C increases as the rotational resistances increase, as would intuitively be expected. The data presented here are all for a seven-node model; however, equivalent results were obtained when the number of nodes was varied.

The buckling analysis also allows plots of the shape of the buckled column to be generated. The buckled column can potentially adopt many different shapes post-failure. Fig. 16 shows two examples of the initial post-buckling modes in the neighbourhood of the first non-trivial bifurcation point for the seven-node model. The displacements of all nodes (q_{xi} and q_{yi}) are very small, and a preferential direction of failure is not clearly identifiable in either the x ((a) and (c)) or y ((b) and (d)) directions. As non-linear sliding will occur once the column starts to buckle, even in very simple systems such as spheres in a DEM simulation or discs in a photoelastic experiment, additional analysis of these buckling modes is perhaps unlikely to provide further insight into the relationship between shear strength and b , which is the focus of the current study.

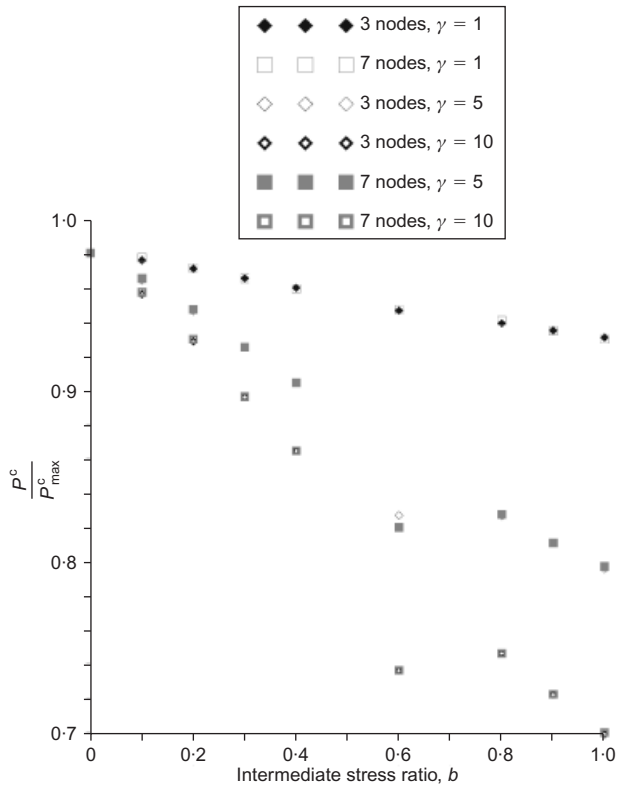


Fig. 14. Normalised buckling load against b for various γ values and rotational stiffnesses of $k_{rx} = k_{ry} = 0.5$

DISCUSSION AND CONCLUSIONS

Although complex, when appropriately analysed, DEM data can give insights into basic mechanisms governing soil behaviour, and allow a hypothesis to be developed. The viability of such hypotheses can be confirmed using analytical models in which the key elements are abstracted for isolated analysis. In this paper DEM simulations of true triaxial tests and a conceptually simple buckling model have been used to argue that the intermediate principal stress influences sand shear strength for the following reasons.

- Failure is associated with buckling of the strong force chains transmitting the major principal stress through the material.
- There is a systematic variation in the support provided by the force network that develops orthogonal to the strong force chains with b .
- This variation in lateral support directly affects the maximum major principal stress (σ_1') that the soil can transmit.

The buckling model is based on the ideas of force-chain buckling that were originally put forward by Oda and his colleagues (e.g. Iwashita & Oda, 1998; Oda & Kazama, 1998; Oda *et al.*, 1998). Tordesillas and her colleagues (Tordesillas & Muthuswamy, 2009; Hunt *et al.*, 2010; Tordesillas *et al.*, 2011) showed that elastic buckling analysis could be applied in a meaningful way to explain some of the phenomena observed in granular materials. Here the authors directly extended the node model proposed by Hunt *et al.* (2010), and applied it to explain the sensitivity of shear strength to b .

It may be possible to develop the buckling model further, and calibrate it to match simulation or physical test data better, or explore the influence of perturbations in the vertical alignment on the result. However, such analyses would perhaps not be appropriate, given that the model is such an abstraction from reality. The role of this model

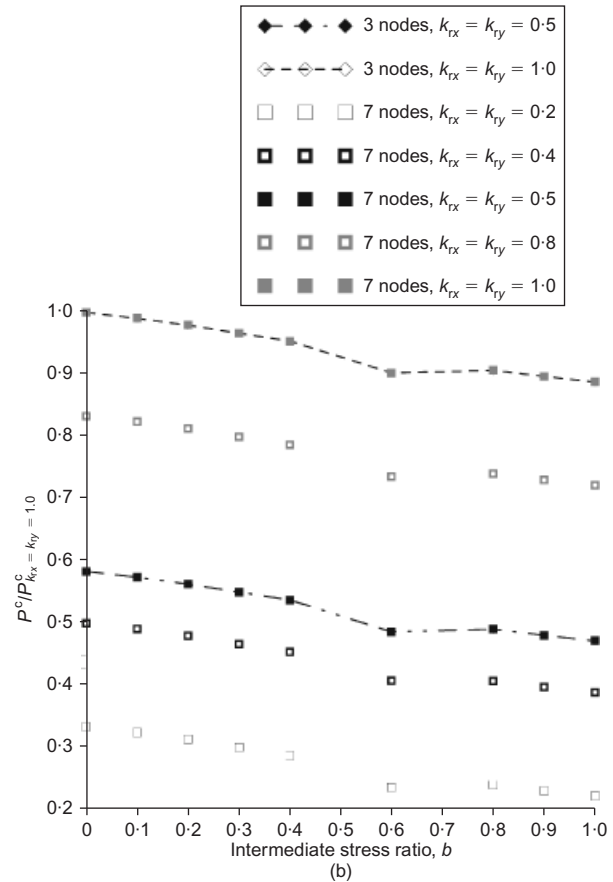
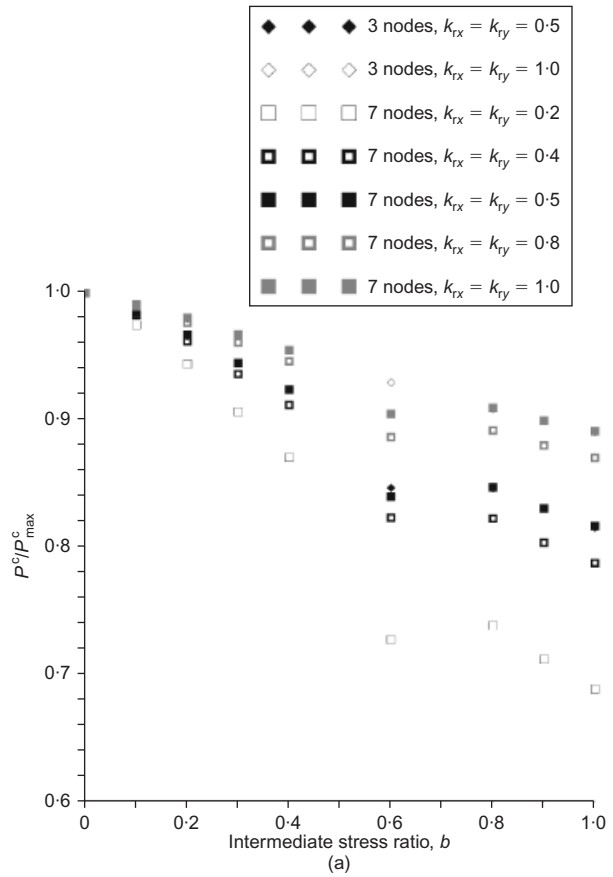


Fig. 15. (a) Buckling load against b for values of $k_{rx} = k_{ry}$ between 0.2 and 1, $\gamma = 5$, normalised by P_{\max} for each value of $k_{ry} = k_{rx}$; (b) absolute buckling load against b for values of $k_{rx} = k_{ry}$ between 0.2 and 1, $\gamma = 5$, normalised by P for $k_{rx} = k_{ry} = 1.0$

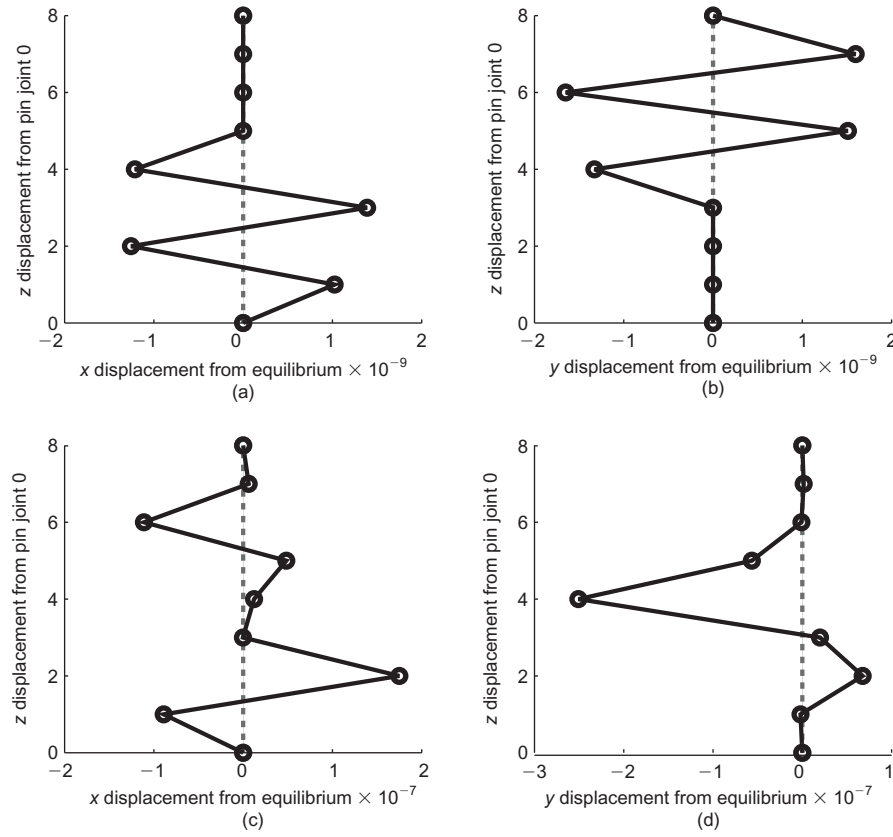


Fig. 16. Representative orthogonal plots of two buckling modes for seven-node model with $b=0.1$ and $k_{rx}=k_{ry}=0.5$. All plots show buckled shape of column as displacement from fixed pin-jointed base against displacement from equilibrium position (when all nodes are collinear). (a), (b) xz and yz projections of column respectively, for one buckling mode; (c), (d) show similar projections for second representative mode. All displacement values normalised by link length L

currently is simply to demonstrate the hypothesis that the relative variation in lateral support to the strong force chains plays a central role in explaining the sensitivity of ϕ' to b . This simple analogue model has pedagogical benefits, and provides a simple, rational explanation to justify the need for 3D models and analyses in geomechanics.

ACKNOWLEDGEMENTS

Financial support for the doctoral research of Dr Barreto was provided by grant EP/D50631X/1 from the Engineering and Physical Sciences Research Council. Dr Hanley is funded as a post-doctoral scholar by the 1851 Royal Commission. The authors appreciate the comments of Dr Jean-Noël Roux and contributions of H. Unterreiner from ENPC, Paris.

NOTATION

b	intermediate stress ratio
d_{50}	mean particle diameter
E_x, E_y	stiffnesses of DEM samples in x - and y -directions respectively
e	void ratio
k_r, k_{rx}, k_{ry}	stiffnesses of linear lateral springs in buckling model
k_r, k_{rx}, k_{ry}	stiffnesses of rotational springs in buckling model
L	length of link between nodes
N	number of nodes in buckling model
N_c^s	number of contacts transmitting forces whose magnitude exceeds the average value
$n_i, i = 1, 2, 3$	unit vector describing contact normal orientation
P	vertical load in buckling model

P^C	critical buckling load in link model
p'	mean effective stress
q_i, q_{ix}, q_{iy}	proportionality factors in buckling model
U_L	elastic potential energy of linear elastic lateral springs
U_R	elastic potential energy of rotational springs
V	total potential energy function
$\alpha_x, \beta_x, \alpha_y, \beta_y$	angles between links in buckling model
γ	proportionality factor
Δ	vertical displacement in buckling model
Δ_i	vertical displacement of i th link in buckling model
ϵ_a	axial strain
$\theta_i, \theta_{xi}, \theta_{yi}$	angle between links in buckling model
μ	interparticle friction
$\Phi_1^s, \Phi_2^s, \Phi_3^s$	strong-force second-order fabric tensor eigenvalues of strong-force second-order fabric tensor
ϕ'	angle of shearing resistance
ϕ'_{peak}	maximum angle of shearing resistance
σ'_1	major principal stress
σ'_2	intermediate principal stress
σ'_3	minor principal stress

REFERENCES

- Barreto, D. (2009). *Numerical and experimental investigation into the behaviour of granular materials under generalised stress states*. PhD thesis, Imperial College of Science, Technology and Medicine, University of London, UK.
- Barreto, D. & O'Sullivan, C. (2012). The influence of inter-particle friction and the intermediate stress ratio on soil response under generalised stress conditions. *Granul. Matter* **14**, No. 4, 505–521.
- Cornforth, D. H. (1964). Some experiments on the influence of

- strain conditions on the strength of sand. *Géotechnique* **14**, No. 2, 143–167, <http://dx.doi.org/10.1680/geot.1964.14.2.143>.
- Cundall, P. & Strack, O. D. L. (1979). A discrete numerical model for granular assemblies. *Géotechnique* **29**, No. 1, 47–65, <http://dx.doi.org/10.1680/geot.1979.29.1.47>.
- Doedel, E. J. & Oldeman, B. E. (2009). *Auto-07p: Continuation and bifurcation software for ordinary differential equations. Technical report*. Montreal, Canada: Department of Computer Science, Concordia University. See <http://indy.cs.concordia.ca/auto/> (accessed 12/07/2013).
- Drescher, A. & de Josselin de Jong, G. (1972). Photoelastic verification of a mechanical model for the flow of a granular material. *J. Mech. Phys. Solids* **20**, No. 5, 337–340.
- Euler, L. (1744). *Methodus inveniendi lineas curvas maximi minimive proprietate gaudentes. Appendix: De curvis elasticis*. Lausanne and Geneva, Switzerland: Marc-Michel Bousquet & Co.
- Haruyama, M. (1981). Anisotropic deformation–strength characteristics of an assembly of spherical particles under three dimensional stresses. *Soils Found.* **21**, No. 4, 41–55.
- Hasan, A. & Alshibli, K. A. (2010). Experimental assessment of 3D particle to particle interaction within sheared sand using synchrotron microtomography. *Géotechnique* **60**, No. 5, 369–380, <http://dx.doi.org/10.1680/geot.2010.60.5.369>.
- Hunt, G. W., Tordesillas, A., Green, S. C. & Shi, J. (2010). Force-chain buckling in granular media: a structural mechanics perspective. *Phil. Trans. R. Soc. A* **368**, No. 1910, 249–262.
- Iwashita, K. & Oda, M. (1998). Rolling resistance at contacts in simulation of shear band development by DEM. *ASCE J. Engng Mech.* **124**, No. 3, 285–292.
- Lade, P. V. (1977). Elasto-plastic stress–strain theory for cohesionless soil with curved yield surfaces. *Int. J. Solids Struct.* **13**, No. 11, 1019–1035.
- Lade, P. V. (1984). Failure criterion for frictional materials. In *Mechanics of engineering materials* (eds C. S. Desai and R. H. Gallagher), pp. 385–402. London, UK: Wiley.
- Lade, P. V. & Duncan, J. M. (1973). Cubical triaxial tests on cohesionless soil. *J. Soil Mech. Found. Div. ASCE* **99**, No. 10, 793–812.
- Lade, P. V. & Duncan, J. M. (1975). Elastoplastic stress–strain theory for cohesionless soil. *J. Geotech. Engng Div. ASCE* **101**, No. 10, 1037–1053.
- Lade, P. V., Nam, J. & Hong, W. P. (2008). Shear banding and cross-anisotropic behaviour observed in laboratory sand tests with stress rotation. *Can. Geotech. J.* **45**, No. 1, 74–84.
- Maplesoft (2011). *Maple v. 15.01*. Waterloo, ON, Canada: Maplesoft.
- Marachi, N. D., Duncan, J. M., Chan, C. K. & Seed, H. B. (1981). Plane-strain testing of sand. In *Laboratory shear strength of soil* (eds R. N. Yong and F. C. Townsend), STP 740, pp. 294–302. West Conshohocken, PA, USA: ASTM International.
- Matsuoka, H. & Nakai, T. (1978). A generalized frictional law for soil shear deformation. *Proceedings of the US–Japan seminar on continuum-mechanical and statistical approaches in the mechanics of granular materials*, Tokyo, Japan, pp. 138–154.
- Ng, T.-T. (2004). Shear strength of assemblies of ellipsoidal particles. *Géotechnique* **54**, No. 10, 659–669, <http://dx.doi.org/10.1680/geot.2004.54.10.659>.
- Oda, M. & Kazama, H. (1998). Micro-structure of shear band and its relation to the mechanism of dilatancy and failure of granular soils. *Géotechnique* **48**, No. 4, 465–481, <http://dx.doi.org/10.1680/geot.1998.48.4.465>.
- Oda, M., Koishikawa, I. & Higuchi, T. (1978). Experimental study of anisotropic shear strength of sand by plane strain test. *Soils Found.* **18**, No. 1, 25–38.
- Oda, M., Kazama, H. & Konishi, J. (1998). Effects of induced anisotropy on the development of shear bands in granular materials. *Mech. Mater.* **28**, No. 1–4, 103–111.
- Ogawa, S., Mitsui, S. & Takemure, O. (1974). Influence of the intermediate principal stress on mechanical properties of a sand. *Proceedings of the 29th annual meeting of JSCE*, Part 3, pp. 49–50. Tokyo, Japan: Japan Society of Civil Engineering.
- Rechenmacher, A., Abedi, S. & Chupin, O. (2010). Evolution of force chains in shear bands in sands. *Géotechnique* **60**, No. 5, 343–351, <http://dx.doi.org/10.1680/geot.2010.60.5.343>.
- Rothenburg, L. & Bathurst, R. (1989). Analytical study of induced anisotropy in idealized granular materials. *Géotechnique* **39**, No. 4, 601–614, <http://dx.doi.org/10.1680/geot.1989.39.4.601>.
- Sadek, T. (2006). *The multiaxial behaviour and elastic stiffness of Hostun sand*. PhD thesis, University of Bristol, UK.
- Satake, M. (1975). Consideration of yield criteria from the concept of metric space. *Technol. Reports Tohoku University* **40**, No. 2, 521–530.
- Shapiro, S. & Yamamuro, J. A. (2003). Effect of silt on three-dimensional stress–strain behaviour of loose sand. *J. Geotech. Geoenviron. Engng* **129**, No. 1, 1–11.
- Sutherland, H. B. & Mesdary, M. S. (1969). The influence of the intermediate principal stress on the strength of sand. *Proceedings of the 7th international conference on soil mechanics and foundation engineering*, Mexico City, Mexico, pp. 391–399.
- Symes, M. J. P. R. (1983). *Rotation of principal stresses in sand*. PhD thesis, University of London, UK.
- Thompson, J. M. T. & Hunt, G. W. (1973). *A general theory of elastic stability*. London, UK: Wiley.
- Thornton, C. (2000). Numerical simulations of deviatoric shear deformation of granular media. *Géotechnique* **50**, No. 1, 43–53, <http://dx.doi.org/10.1680/geot.2000.50.1.43>.
- Thornton, C. & Antony, S. J. (1998). Quasi-static deformation of particulate media. *Phil. Trans. R. Soc. A* **356**, No. 1747, 2763–2782.
- Tordesillas, A. (2007). Force chain buckling, unjamming transitions and shear banding in dense granular assemblies. *Phil. Mag.* **87**, No. 32, 4987–5016.
- Tordesillas, A. & Muthuswamy, M. (2009). On the modeling of confined buckling of force chains. *J. Mech. Phys. Solids* **57**, No. 4, 706–727.
- Tordesillas, A., Shi, J. & Tshaiwsky, T. (2011). Stress–dilatancy and force chain evolution. *Int. J. Numer. Analyt. Methods Geomech.* **35**, No. 2, 264–292.